JGR Atmospheres

RESEARCH ARTICLE
10.1029/2018JD029849

Water Vapor, Clouds, and Saturation in the Tropical Tropopause Layer

M. R. Schoeberl[1], E. J. Jensen[2], L. Pfister[2], R. Ueyama[2], T. Wang[3,4], H. Selkirk[3,5], M. Avery[6], T. Thornberry[7], and A. E. Dessler[8]

[1]Science and Technology Corporation, Columbia, MD, USA, [2]NASA Ames Research Center, Moffett Field, CA, USA, [3]Goddard Space Flight Center, Greenbelt, MD, USA, [4]Earth System Science Interdisciplinary Center, University of Maryland, College Park, MD, USA, [5]Universities Space Research Association, Columbia, MD, USA, [6]NASA Langley Research Center, Hampton, VA, USA, [7]NOAA Earth System Research Laboratory, and Cooperative Institute for Research in Environmental Sciences, University of Colorado Boulder, Boulder, CO, USA, [8]Department of Atmospheric Sciences, Texas A&M University, College Station, TX, USA

Key Points:
- Aircraft, balloon, and satellite measurements show that the upper tropical troposphere layer has persistent high humidity
- The high humidity is due to both adiabatic and diabatic upward vapor transport into the cold upper troposphere leading to cloud formation
- Convection is not important in maintaining the high humidity environment

Correspondence to:
M. R. Schoeberl,
mark.schoeberl@mac.com

Citation:
Schoeberl, M. R., Jensen, E. J., Pfister, L., Ueyama, R., Wang, T., Selkirk, H., et al. (2019). Water vapor, clouds, and saturation in the tropical tropopause layer. *Journal of Geophysical Research: Atmospheres*, *124*, 3984–4003. https://doi.org/10.1029/2018JD029849

Received 16 OCT 2018
Accepted 6 MAR 2019
Accepted article online 18 MAR 2019
Published online 1 APR 2019

Author Contributions:
Conceptualization: M. R. Schoeberl, E. J. Jensen, R. Ueyama
Data curation: M. R. Schoeberl, L. Pfister
Formal analysis: M. R. Schoeberl
Funding acquisition: M. R. Schoeberl, A. E. Dessler
Investigation: M. R. Schoeberl, R. Ueyama, M. Avery
Methodology: M. R. Schoeberl, T. Wang, M. Avery, A. E. Dessler
Project administration: A. E. Dessler
Software: M. R. Schoeberl, T. Wang, T. Thornberry
Supervision: A. E. Dessler
Validation: M. R. Schoeberl, T. Thornberry
Writing - original draft: M. R. Schoeberl
Writing – review & editing: E. J. Jensen, L. Pfister, R. Ueyama, T. Wang, M. Avery, A. E. Dessler

Abstract The goal of this investigation is to understand the mechanism behind the observed high relative humidity with respect to ice (RHi) in the tropical region between ~14 km (150 hPa) and the tropopause, often referred to as the tropical tropopause layer (TTL). As shown by satellite, aircraft, and balloon observations, high (>80%) RHi regions are widespread within the TTL. Regions with the highest RHi are colocated with extensive cirrus. During boreal winter, the TTL RHi is highest over the Tropical Western Pacific (TWP) with a weaker maximum over South America and Africa. In the winter, TTL temperatures are coldest and upward motion is the greatest in the TWP. It is this upward motion, driving humid air into the colder upper troposphere that produces the persistent high RHi and cirrus formation. Back trajectory calculations show that comparable adiabatic and diabatic processes contribute to this upward motion. We construct a bulk model of TWP TTL water vapor transport that includes cloud nucleation and ice microphysics that quantifies how upward motion drives the persistent high RHi in the TTL region. We find that atmospheric waves triggering cloud formation regulate the RHi and that convection dehydrates the TTL. Our forward domain-filling trajectory model is used to more precisely simulate the TTL spatial and vertical distribution of RHi. The observed RHi distribution is reproduced by the model, and we show that convection increases RHi below the base of the TTL with little impact on the RHi in the TTL region.

Plain Language Summary Satellite, aircraft, and balloon observations show that the upper tropical tropospheric humidity is close to saturation. This high humidity is the result of the near-continuous upward movement of water vapor from the midtroposphere into the colder upper troposphere that results in extensive cirrus formation. Bulk and trajectory model simulations show how this process works and that convective injection of water into the tropical upper troposphere is relatively unimportant.

1. Introduction

The boreal winter (December–February [DJF]) Tropical Western Pacific (TWP) tropical tropopause layer (TTL, ~14–18 km) exhibits some of the coldest temperatures in the lower atmosphere (e.g., Fueglistaler et al., 2009; Seidel et al., 2001) with relative humidities with respect to ice (RHi) that are near or above saturation (Jensen et al., 1999; Jensen, Thornberry, et al., 2017). Regions of high winter tropical RHi regions in the TTL are also observed over South/Central America (Krämer et al., 2009; Vömel et al., 2002). In boreal summer (June–August [JJA]), regions of high RHi regions are found over Central America (Selkirk et al., 2010) and Africa (Khaykin et al., 2009) as well as in the regions of the North American and the Himalaya monsoons (Randel & Jensen, 2013; Vömel et al., 2002). Persistent cirrus occurs in these high RHi regions (e.g., Pfister et al., 2001; Sassen et al., 2009). These cirrus decks significantly impact the incoming and outgoing radiation (Haladay & Stephens, 2009) that are not well represented in climate models (Boucher et al., 2013; Intergovernmental Panel on Climate Change, 2013). Potential changes in the TTL cirrus and water vapor fields as the climate changes may alter the radiation budget as a feedback (Zhou et al., 2014). For example, as the climate warms an increase in the penetration of convective systems into the TTL might increase cirrus formation and stratospheric water vapor (Dessler et al., 2016).

The dehydration of air moving into the stratosphere requires cirrus formation in the tropical upper troposphere and by implication RHi values near saturation. Observations of high RHi in the TWP TTL were seen in early aircraft, balloon, and satellite measurements (Gettelman et al., 2002; Jensen et al., 1999; Newell et al., 1996; Vömel et al., 2002). Commercial aircraft observations also show high RHi in the lower TTL (Zahn et al., 2014). More recent high-altitude aircraft observations of the winter west Pacific observations made by the National Aeronautics and Space Administration (NASA) Airborne Tropical TRopopause EXperiment (ATTREX, Jensen, Pfister, et al., 2017) and the Pacific Oxidants, Sulfur, Ice, Dehydration, and cONvection (POSIDON) missions recorded RHi values as high as 160% (Jensen, Thornberry, et al., 2017).

Jensen et al. (2001) suggested that in the lower TTL TWP region, saturated air is maintained by a combination of deep convection transporting water vapor into the TTL and overall rising motion. Radiative transfer calculations show that the TTL is out of radiative equilibrium with net diabatic heating and upward motion above 15–16 km (Randel & Jensen, 2013; Yang et al., 2010) and extending into the stratosphere. As moist air moves upward toward the tropopause and temperature decreases, RHi increases and there is a higher probability of cloud formation (Jensen et al., 1999). In fact, Corti et al. (2006) argued that inclusion of TTL clouds in the radiative transfer models would significantly increase the vertical range and magnitude of the net diabatic heating. Holton and Gettelman (2001) and Gettelman et al. (2002) argued that it is primarily the horizontal advection of air into the coldest parts of the TTL, usually over the TWP, that produces high RHi and persistent cirrus. Their simulations reproduced the formation of cirrus at the edge of the coldest parts of the TWP as was observed by the Halogen Occultation Experiment (Russell et al., 1993). Clearly, both diabatic heating and horizontal transport play a role in defining the structure of the RHi distribution, and we quantify their contributions below.

The DJF TWP region is a region marked by intense convection (Liu & Zipser, 2005). Convection plays two roles: altering the dynamics of the TTL TWP region and supplying water to the TTL. The linkage between TWP cold temperatures, convection, and the water vapor distribution is not surprising (Randel et al., 2003). The observed spatial structure of the TWP TTL cold region and the associated dipole circulation is a Matsuno-Gill response to the latent heat released by convective clusters in the south of the equator (Gill, 1980; Kim et al., 2018). Basically, the convective heating forces stationary Rossby and Kelvin waves, which creates a larger cold pool that straddles the equator somewhat east of the convective centers. This cold pool is relatively shallow compared to the underlying warm anomalies because of the change in static stability at the tropopause (see Kim et al., 2018, Figure 6).

It is well understood that convection is the primary source of water in the midtroposphere (Corti et al., 2006; Folkins et al., 2002; Minschwaner & Dessler, 2004; Romps, 2014) and convection is occasionally observed to detrain even above the tropopause (e.g., Avery et al., 2017; Corti et al., 2008; Kelly et al., 1993; Wang & Dessler, 2012). There is clear evidence that it is playing a role in the TTL's water vapor budget, both in direct measurements of water vapor (Schoeberl et al., 2018; Ye et al., 2018) and in other tracers, such as HDO (Dessler et al., 2007; Moyer et al., 1996).

Convection, however, cannot supersaturate the air (Jensen et al., 2007; Schoeberl et al., 2018) because the presence of convective ice in equilibrium automatically limits the ambient RHi to 100%. The only process that can produce supersaturation is the additional cooling of saturated air. Furthermore, this cooling must take place without abundant effective ice nuclei. Africa and South America are also the locus of strong winter convection associated with the diurnal cycle of surface heating (Carminati et al., 2014; Johnston et al., 2018; Khaykin et al., 2013). These regions will be the subject of future analyses.

Although in this paper we focus mostly on the winter TWP, the tropical eastern Pacific (TEP) is interesting in contrast to the TWP. The TEP has relatively lower RHi (Jensen et al., 1999; Jensen, Thornberry, et al., 2017; Vömel et al., 2002), fewer clouds (Sassen et al., 2009), and infrequent convective events (Liu & Zipser, 2005). Newell et al. (1996) suggested that the winter Walker circulation, which produces a subsiding, warming circulation, would reduce the RHi in the TEP TTL.

In this paper, we analyze observations from a variety of sources to provide a more comprehensive picture of the TTL RHi structure and the role of convection. In order to understand the dynamics of the TTL, we use a bulk model to simulate TTL RHi similar to that used by Jensen et al. (2001) and

explore the role of waves and simplified convection on TTL RHi. We also revisit the horizontal advection process first described by Holton and Gettelman (2001) and further described by Ueyama et al. (2015). Using back trajectories, we quantify the contribution of adiabatic (motion along the sloping potential temperature isentropes, e.g., Pfister et al., 2001) and diabatic motion (motion across the isentropes) to the vertical motion field. Finally, we use our forward domain-filling (FDF) trajectory model (Schoeberl & Dessler, 2011) to provide additional information on the role of convection in maintaining the TTL RHi.

2. Observational Data Sets

Our observational data sets include satellite, aircraft, and balloon measurements in both TWP and TEP during DJF and JJA periods. The satellite limb sounding data sets provide excellent horizontal and temporal coverage but lower vertical resolution and fewer measurement types than the aircraft platforms. Balloonsonde data sets provide high vertical resolution, multiyear coverage at the same location for a few measurements. All three observation types are highly complementary.

2.1. Satellite Observations

In order to map the extent of the saturated TTL region, we use Microwave Limb Sounder (MLS) V4.2 measurements of water vapor (see Livesey et al., 2017) along with temperatures from the Modern-Era Retrospective analysis for Research and Applications, Version 2 (MERRA2), which uses GEOS5 as the atmospheric general circulation model (Gelaro et al., 2017; Molod et al., 2015) to compute the RHi over ice. The pressure and temperature dependence of the ice saturation mixing ratio comes from Murphy and Koop (2005). RHi is also an MLS product (hereafter MLS-RHi). We have compared RHi using MERRA2 temperatures with MLS-RHi and find that MLS-RHi is on the average about 4% higher at 100 hPa in the TTL. The source of this RHi bias appears result from the MLS cold temperature bias (Livesey et al., 2017) compared to reanalysis. We have also compared RHi spatial patterns using both our RHi and MLS-RHi and find no significant differences.

For cloud fraction (CF) we use both day and night Cloud-Aerosol Lidar with Orthogonal Polarization (CALIOP) V4 cloud profiles (CPro) in 5-km horizontal resolution (see https://www.atmos-meas-tech.net/special_issue903.html).

To compute the local CF, we grid CALIOP data into volumes of 4° by 8° latitude-longitude boxes with approximately 1.34 km in depth centered on the MLS pressure levels and extending to half way between the adjacent levels. For each grid box volume, the CALIOP feature mask is used to determine the presence of clouds. The CF defined here is the number of observations indicating cloud divided by the total number of observations made in the same volume over a monthly period.

In addition to the CALIOP CF, we use the satellite convective (SC) height data set described by Ueyama et al. (2015) and Schoeberl et al. (2018) and produced by L. Pfister (personal communication, 2014, see Acknowledgments for data set access). The SC convective cloud tops are determined by combining precipitation estimates with infrared (IR) brightness temperatures (equivalent blackbody temperatures) from geostationary satellites. The precipitation estimates are obtained from the Tropical Rainfall Measuring Mission (TRMM) version 3B42RT in 0.25° × 0.25° spatial and 3-hourly temporal resolution (Huffman et al., 2010). Brightness temperature is obtained from the NCEP/CPC 4-km Global (60°N to 60°S) IR data set. The detection algorithm first identifies grid cells with precipitation rates exceeding predefined thresholds (~1 mm/hr) indicating possible convection and then uses the coincident IR effective brightness temperature to determine cloud top pressure. Reanalyses are used to compute the potential temperature. Note that the effective brightness temperature is adjusted by an offset due to the fact that IR methods underestimate the cloud top altitude by about 1 km (Sherwood et al., 2004). The SC data set remains to be extensively validated, but convective cloud top heights match CALIOP measurements taken at appropriate local times, are consistent with radar data taken over the continental United States (Cooney et al., 2018), and the global cloud top height statistics appear to be spatially consistent with MERRA model convective fields, although consistently higher in altitude (Schoeberl et al., 2018).

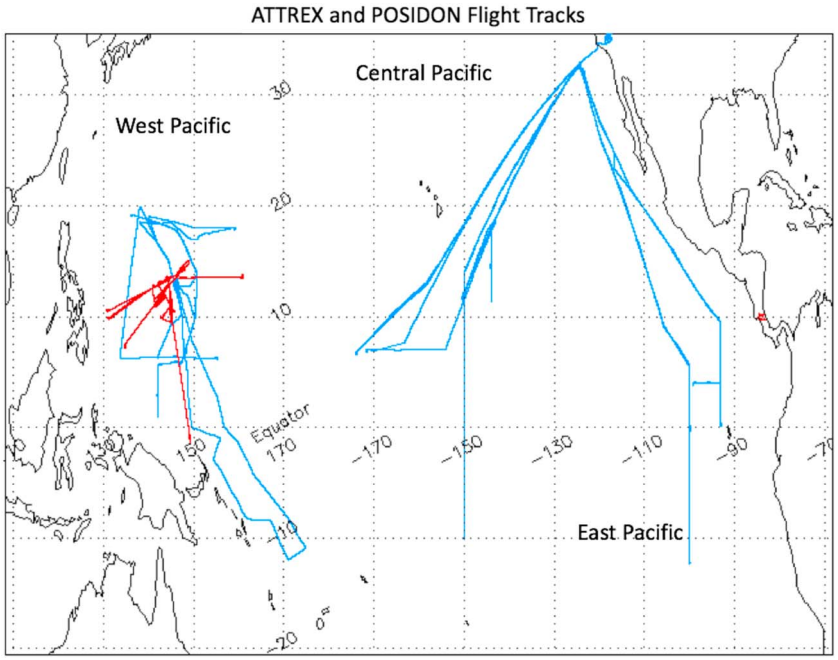

Figure 1. Flight tracks for data aircraft data used in this study. ATTREX flights are in blue, and POSIDON flights are in red. Red star indicates the location of the Costa Rica Ticosonde launches. ATTREX = Airborne Tropical TRopopause EXperiment; POSIDON = Pacific Oxidants, Sulfur, Ice, Dehydration, and cONvection.

2.2. Aircraft Observations

For this study, we use the high-altitude TWP and TEP observations from ATTREX (Jensen, Pfister, et al., 2017) and TWP observations from POSIDON. While the aircraft measurements are not uniform within the tropical upper troposphere and lower stratosphere, they provide corroborating and complementary measurements to the satellite data. The aircraft water vapor measurements will have much higher vertical resolution than MLS, and the ice crystal data will allow us to composite in-cloud and out-of-cloud data more easily than with MLS observations.

ATTREX measurements were made during late boreal winter, flying from NASA Armstrong Flight Research Center into the TEP and central Pacific (2013) and from Guam into the TWP the following year. The data can be found at https://espoarchive.nasa.gov/archive/browse/attrex. POSIDON measurements were made mostly in the TWP during October 2016. The POSIDON mission description and data archive can be found at https://espo.nasa.gov/posidon. In both missions, the aircraft carried cloud particle detectors and water vapor instruments and made meteorological measurements. Water vapor measurements used here were obtained by the NOAA-H_2O two-channel, internal-path tunable diode laser hygrometer that can measure both vapor and total water (Thornberry et al., 2015); the difference between total water and vapor is due to ice. The ATTREX RHi and cloud measurements have been described by Jensen, Thornberry, et al. (2017) and Woods et al. (2018) who showed that extensive supersaturation was observed in the TWP outside of cloud, and inside clouds, the RHi is on the average 100% although occasionally supersaturation and subsaturation were observed inside cirrus.

In compositing the data, we used ATTREX flights on (YYYY/MM/DD) 2013/02/05, 2013/02/09, 2013/02/14, 2013/02/21, 2013/02/26, and 2013/03/01 for the TEP and central Pacific, and we used data from ATTREX flights on 2014/02/12, 2014/03/04, 2014/03/06, and 2014/03/09 and POSIDON flights on 2016/10/12, 2016/10/14, 2016/10/15, 2016/10/18, 2016/10/19, 2016/10/21, and 2016/10/25 for the TWP. Flights were selected based on data availability throughout the flight. Figure 1 shows the flight tracks, ATTREX in blue and POSIDON in red. We note that POSIDON occurred during the transition season between JJA and DJF, and only one of the ATTREX TWP flights actually occurred in the DJF period, but the data showed that even just outside of winter period, the TWP TTL RHi is quite high. In order to connect to the aircraft observation

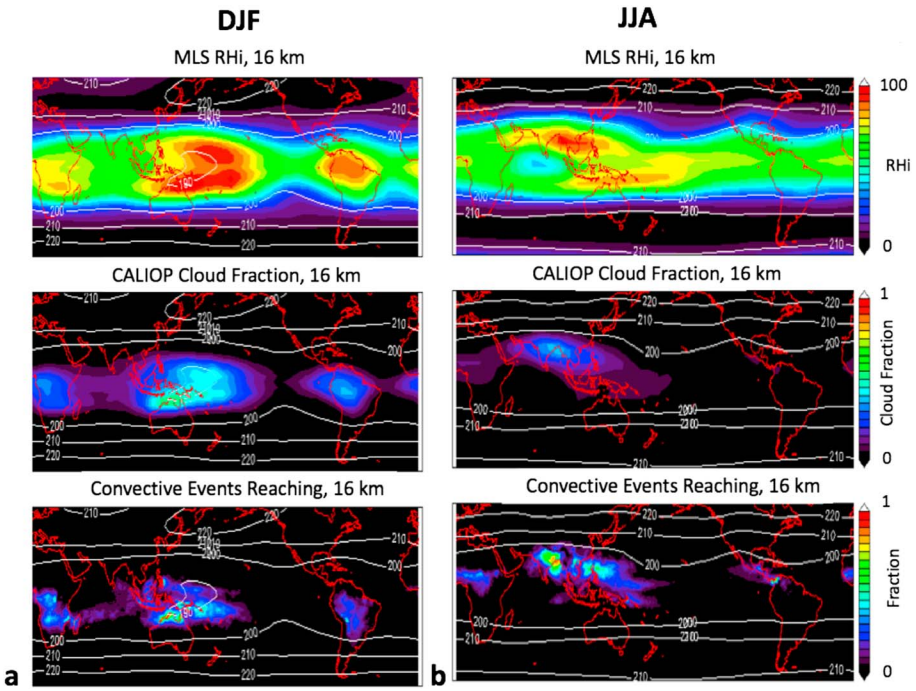

Figure 2. Eight-year averaged fields at the MLS 100-hPa level (~16 ± 0.66 km) for (a) boreal winter (DJF) and (b) boreal summer (JJA). Within each part, the top panel shows the RHi computed using MLS water vapor and colocated MERRA2 temperatures; the middle panel the CALIOP cloud fraction computed for 4° × 8° bins (see text) at the MLS level ± 0.66 km; and the bottom panel the number of convective systems reaching 16 km or higher normalized by the maximum number found in each 1° × 1° grid cell. White contours are the 8-year average MERRA2 temperatures at 100 hPa. CALIOP = Cloud-Aerosol Lidar with Orthogonal Polarization; MLS = Microwave Limb Sounder; RHi = relative humidity with respect to ice; DJF = December–February; JJA = June–August.

with the satellite data, we have interpolated daily MLS water vapor data onto the aircraft flight track and performed identical compositing with the MLS data.

2.3. Water Vapor Sonde Observations

The balloon data we use is the Ticosonde data set (Selkirk et al., 2010), which provides a relatively long record of water vapor soundings over Costa Rica (10°N, 84°W see Figure 1 for the location). The Ticosonde data are used to contrast JJA and DJF profiles in the East Pacific. Water vapor mixing ratio profiles are obtained using the cryogenic frostpoint hygrometer (Vömel et al., 2007). We use the data from 2005 to 2011 to create a climatology of the TTL over Costa Rica. During this period, sondes were typically launched at ~1800 UT, close to the Aura MLS and CALIPSO overpass time. The sonde water vapor profiles are composited into DJF and JJA as with the other data sets above, and we only consider sondes that reach 22 km to make sure we cover the entire TTL region. For the winter period, 20 sondes are used; for the summer period, 24 sondes are used. For each of the sonde launches we interpolate MLS RHi to the sonde site and composite those profiles as well for comparison.

3. Analysis of Observations

3.1. Satellite Measurements

Figure 2 shows DJF 8-year average maps (2006–2014) of 100-hPa (~16-km) RHi, temperatures, CF, and the normalized number of convective systems reaching 16 km averaged onto a 1° × 1° grid. The regions with the highest RHi are coincident with the highest CF and coldest temperatures. However, the regions with highest occurrence of deep convection are not entirely concentrated in the regions with the highest CF in the boreal winter TWP and over South America. This supports the idea that the winter CF is a mixture of convective and stratiform cirrus, mostly the latter.

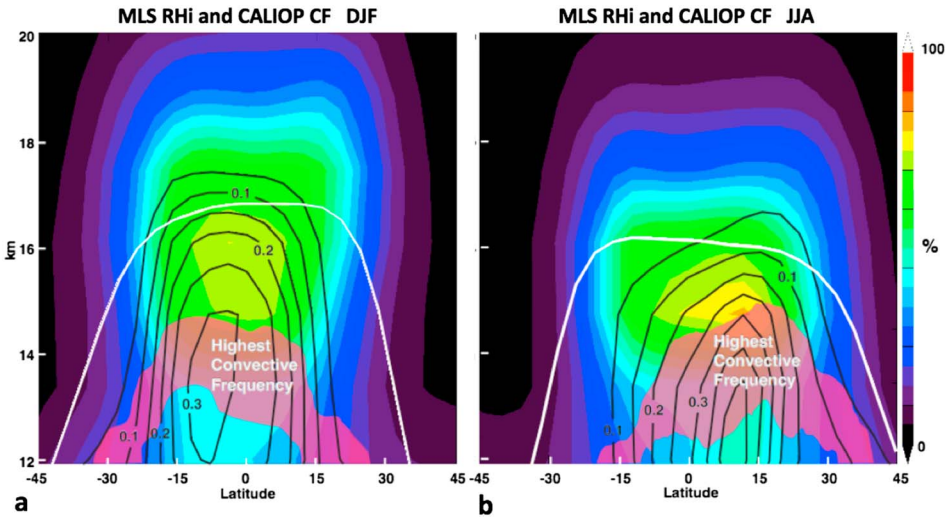

Figure 3. Zonal mean RHi (color). Black contours indicate the zonal mean CALIOP cloud fraction, and the red band shows the zone of the highest density of satellite convective tops; thick white line is the zonal mean tropopause. (a) DJF. (b) JJA. CALIOP = Cloud-Aerosol Lidar with Orthogonal Polarization; CF = cloud fraction; MLS = Microwave Limb Sounder; RHi = relative humidity with respect to ice; DJF = December–February; JJA = June–August.

Figure 3 shows the zonal mean distribution of RHi, CF, and the zone where the highest frequency of convective systems reaching TTL altitudes occurs. The highest convective frequency is basically the regions with high probability of convection reaching a given altitude. The procedure is as follows: For the target period, the average convective altitude is computed for each 1° by 1° grid bin (as shown in Figure 2c). For each latitude bin, the number of longitude bins with convection reaching a given altitude is counted. For this work, we identify highest convective frequency as greater than 20% probability of systems reaching a given altitude.

For DJF, the zone of maximum RHi (about 16 km) is well above both the highest convective frequency and the peak in the CF. This suggests convective moistening has a direct impact only in the lower part of the TTL but less important when moving upward to the tropopause (Ueyama et al., 2018). Convection does occasionally reach the tropopause, but from a statistical perspective, the impact of convection on water vapor is decreasingly important in the upper TTL (Schoeberl et al., 2018). We will return to this point below. It is important to recognize that our focus here is on the water vapor budget, cloud formation, and the role of convection in supplying water vapor. Convection reaching lower altitudes can indirectly influence the TTL by reducing the tropopause temperature through a dynamic response even if the convective system does not reach the TTL (Kim et al., 2018).

For JJA, in contrast to DJF, the zone of maximum RHi and peak convective frequency have a closer correspondence. Both the most humid region and the top of the convective layer occurs at ~15°N. The CF peak is somewhat lower but at the same latitude. This suggests that the TTL RHi during JJA can be attributed to convective moistening (Ueyama et al., 2018).

We find that it is useful to quantify the RHi statistics throughout the TTL region. At each log-pressure altitude, a normalized probability density function (PDF) of the MLS RHi observations is constructed for the latitudes <20°. This distribution includes near-saturated regions over the TWP and continents as well as drier regions such as the TEP and Atlantic Ocean. Figure 4 shows the resulting two-dimensional PDF. The RHi shows a backward C pattern with most RHi values below 50% at altitudes below 14 km and RHi values rising toward 100% at altitudes above 14 km. The CF PDF shows little change with altitude below 15 km. Both RHi and CF fall off above the tropopause into the stratosphere where temperatures warm. The dotted line in the figure shows the frequency occurrence of convective tops with altitude. As discussed above (Figure 3), the convective frequency is high in the very lowest part of the TTL but drops off quite rapidly with altitude. At 16 km, for example, the CF remains high, but the convective frequency is very low, suggesting that stratiform cirrus dominates the CF near16 km.

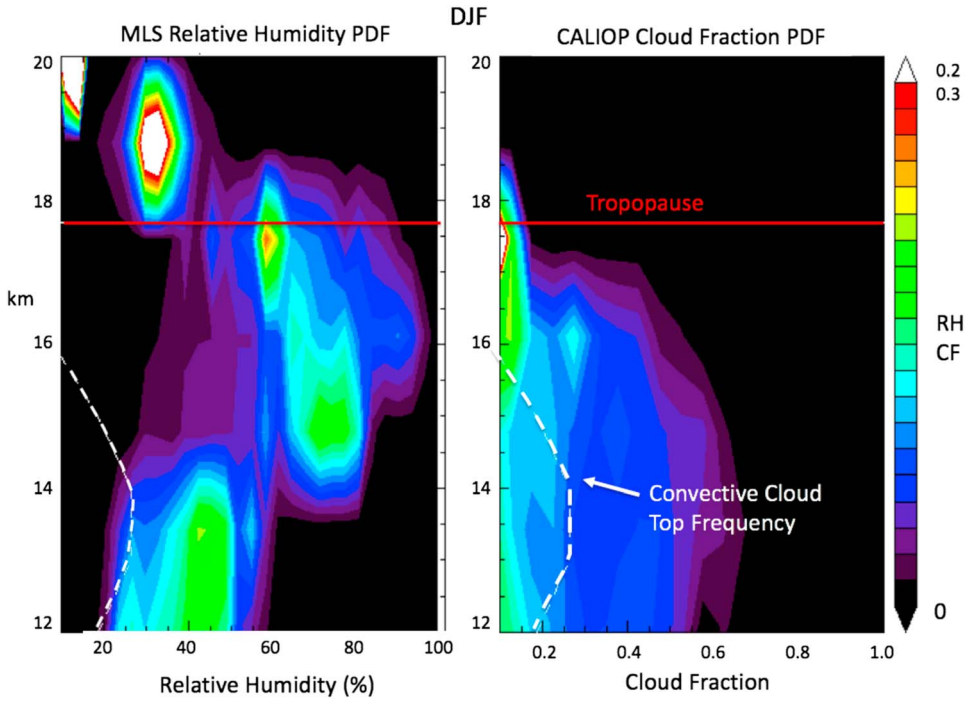

Figure 4. Tropical (latitude < 20°) RHi normalized PDF (left) and CF normalized PDF (right) using data shown in Figures 2a and 3a (DJF). White dashed lines show the SC relative convective top frequency; solid line shows the maximum tropopause height. The scale for RH goes to 0.2, while the scale for CF extends to 0.3. MLS = Microwave Limb Sounder; PDF = probability density function; CALIOP = Cloud-Aerosol Lidar with Orthogonal Polarization; RH = relative humidity; CF = cloud fraction.

3.2. Aircraft Observations

3.2.1. TWP TTL

Figure 5 shows a PDF analysis of the aircraft observations and MLS observations interpolated along the aircraft tracks. Figure 5a shows the RHi composited from the TWP aircraft data; the PDF has been slightly smoothed. Figure 5b shows the results when rejecting observations in the presence of clouds; this reduces the concentration of points near 100% RHi as expected. The backward C shaped pattern seen in Figure 3 (MLS data) is clearly evident in the aircraft observations. In the TWP, both Figures 5a and 5b show that the saturated TTL begins above ~13.5 km and extends to the tropopause. The tropopause moves up and down along the flight tracks and somewhat blurs the distribution compared to composites in tropopause relative coordinates. Figure 5c shows MLS RHi from measurements collocated to the flight tracks. The colocated MLS RHi values are somewhat lower than the aircraft observations below 15 km, but this is not surprising given the lower vertical resolution of the satellite data. In addition, the MLS data are known to be dry biased at lower altitudes (Livesey et al., 2017).

3.2.2. Tropical Eastern Pacific TTL

Figure 2 shows that both the RHi, CF, and convective frequency are much lower in the TEP than in the TWP. Figure 6 shows the composite of TEP aircraft measurement RHi and along track MLS measurements. In contrast to Figure 5 (the TWP) the TEP RHi is relatively lower at all levels, but an increase in RHi with altitude does occur above 14 km. Because the TEP has fewer clouds, the difference between the “all data” and “no-cloud” cases (Figures 6a and 6b) is small, as was also found in Jensen, Thornberry, et al. (2017).

3.3. Water Vapor Sonde Observations

3.3.1. Winter TTL

An analysis of the Ticosonde data is shown in Figure 7. The comparison of cryogenic frostpoint hygrometer measurements with MLS shown in Figure 7a indicates that both data sets provide a similar picture. RHi increases above 14 km with some supersaturation evident above about 15.5 km up to the average tropopause (red line). The Costa Rica winter profiles are similar to the TEP profiles in Figure 6, but winter Costa Rica

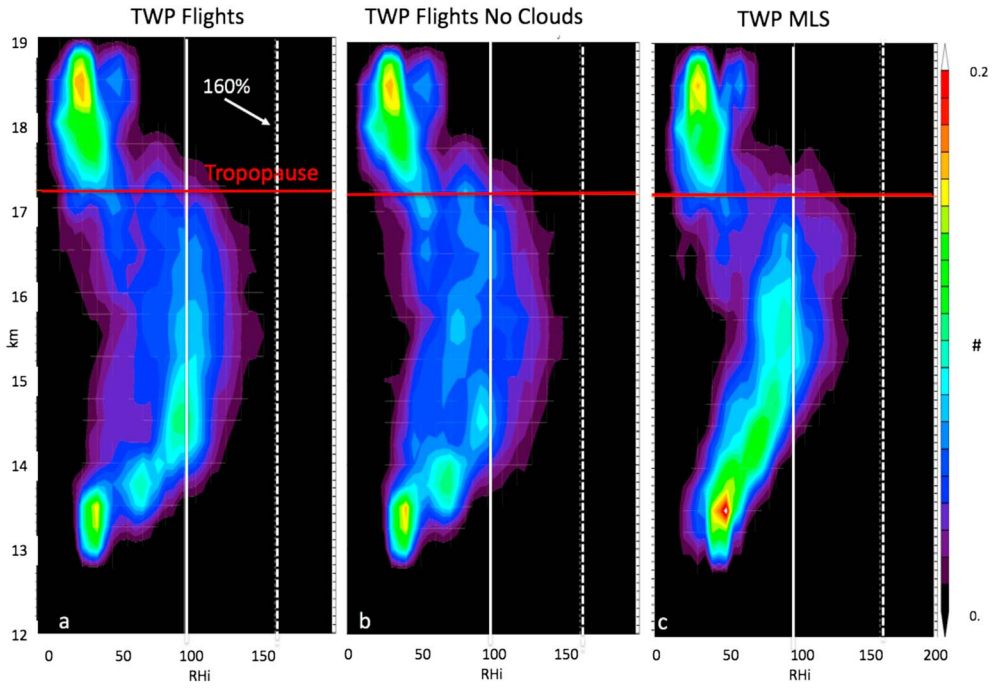

Figure 5. Composite aircraft and satellite normalized probability density function of TWP cloud fraction and RHi observations within 20° of the equator from Pacific Oxidants, Sulfur, Ice, Dehydration, and cONvection and Airborne Tropical TRopopause EXperiment along with MLS measurements interpolated to flight tracks. Solid white line is 100% RHi, while dashed line is 160% RHi (see arrow). Red line is the average tropopause height. (a) All flights (see text). (b) All flights except the data where clouds are present is removed. (c) Composited collocated MLS measurements interpolated to the flight tracks. TWP = Tropical Western Pacific; MLS = Microwave Limb Sounder; RHi = relative humidity with respect to ice.

profiles exhibit more near-saturation events. Selkirk et al. (2010) noted that these saturation events were likely associated with wave-induced clouds, possibly generated by the mountainous topography near the San Jose launch site.

3.3.2. Summer TTL

The summer Costa Rica profiles (Figure 7b) show a quite different structure, with a low tropopause and a concentration of measurements near 100% RHi. There is often strong local convection over Costa Rica in the summer and the 100% RHi measurements suggest convective influence up to 15 km. Figure 2b also indicates nearby convection with cloud tops near 15 km. In contrast, the MLS fields show lower RHi below 16 km. This may be due to the interpolation from MLS measurements over the ocean to the land location or dry bias in the MLS retrievals.

4. Dynamics of the Tropical TTL

The observations (Figures 4–7) all show increasing RHi above 14 km associated with colder temperatures with a sharp decrease in RHi above the tropopause moving into the warmer stratosphere. The spatial pattern (Figure 2) also mirrors this temperature correlation. Over the TWP, and to a lesser extent over the TEP, supersaturation is frequently present in the upper TTL (Jensen, Thornberry, et al., 2017; Rollins et al., 2016).

One simple explanation for the existence of the saturated TTL is that water vapor deposited by convection below ~14–15 km is being advected upward by diabatic processes into the cold upper troposphere. Since water vapor is conserved and the temperature decreases with altitude, RHi will increase above 100% (Jensen et al., 2001). Eventually, the RHi exceeds the nucleation threshold (~160% for homogeneous nucleation, lower for heterogeneous nucleation). At the nucleation threshold, clouds form, and ice crystals grow quickly and fall through the layers below (consistent with CF shown in Figures 2–4). Falling ice crystals continue to grow as they fall, and they remove water vapor from supersaturated layers before finally evaporating

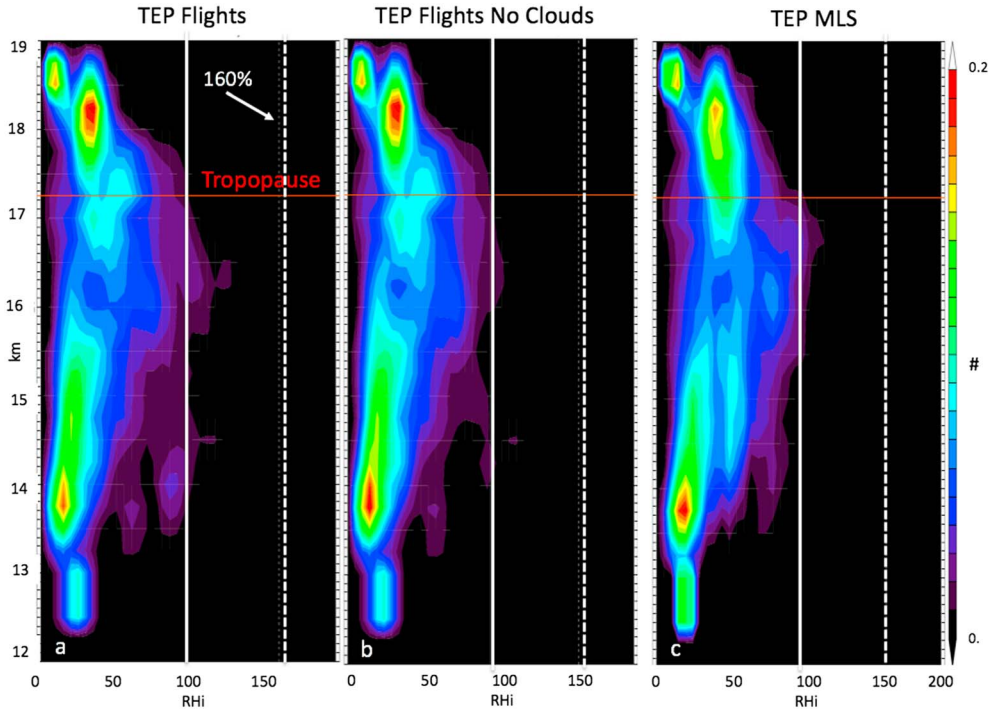

Figure 6. As in Figure 5, composite probability density functions of TEP aircraft RHi observations within 20° of the equator from POSIDON and ATTREX along with MLS measurements. Thin white line is 100% RHi, while dashed line is 160% RHi. Red line is the average tropopause height. (a) All flight (see text). (b) All flights except the data where clouds are present is removed. (c) Composited collocated MLS measurements interpolated to the flight tracks. TEP = tropical eastern Pacific; MLS = Microwave Limb Sounder; RHi = relative humidity with respect to ice.

in the subsaturated layers below the condensation level. The upward advection provides continued replenishment of vapor that is removed by ice formation. In other words, vertical motion supplies water vapor, which is constantly depleted as falling ice.

In addition to diabatic motion, upward transport of water vapor can also come from adiabatic lifting (Holton & Gettelman, 2001). Since the TWP TTL is colder than the surrounding region, air being advected horizontally will ride up the potential temperature isentropes and cool as it enters the TWP. The cooling increases the RHi, which in turn increases the probability of cloud formation (Pfister et al., 2001). Exiting the TWP region, adiabatic motion down the isentropes warms the air and lowers the RHi. Cloud formation is less likely.

In order to create the observed TTL distribution of water vapor and clouds, both the adiabatic and diabatic upward motions need to drive air upward into the colder upper troposphere. To determine the relative scales of the adiabatic and diabatic lifting process we compute the diabatic and adiabatic components of the w field using reanalyses. We do this by computing the change in trajectory parcel log pressure height (z), where $z = H \log\left(\frac{p_o}{p}\right)$, p is the pressure, p_o is the surface pressure, and H is the scale height (~7 km). We can then estimate the vertical velocity, $w(t) = (z_f(t+\Delta t) - z_b(t-\Delta t))/2\Delta t$, where z_f is z at the forward trajectory points and z_b is z at the backward trajectory points. We use $\Delta t = 2$ days. This method is a variant on the reverse domain-filling method (Schoeberl & Newman, 1995). The vertical velocity consists of diabatic and adiabatic components, w_d and w_a. To compute the adiabatic component, w_a, we set the diabatic heating rate to 0 and recompute w, this is the adiabatic component, w_a. The diabatic component, w_d, is $w - w_a$.

Figure 8 shows w, w_a, and w_d averaged over 2006–2010 for DJF at 370 K (~107 hPa) for the TWP region using both ERA-Interim (ERAi, Dee et al., 2011) and MERRA2 reanalysis. The wind vectors indicate the location of a pair of high pressure systems, one located just west of 180° longitude, north of the equator, and one over Australia south of the equator. These two systems are a result of the Matsuno-Gill response

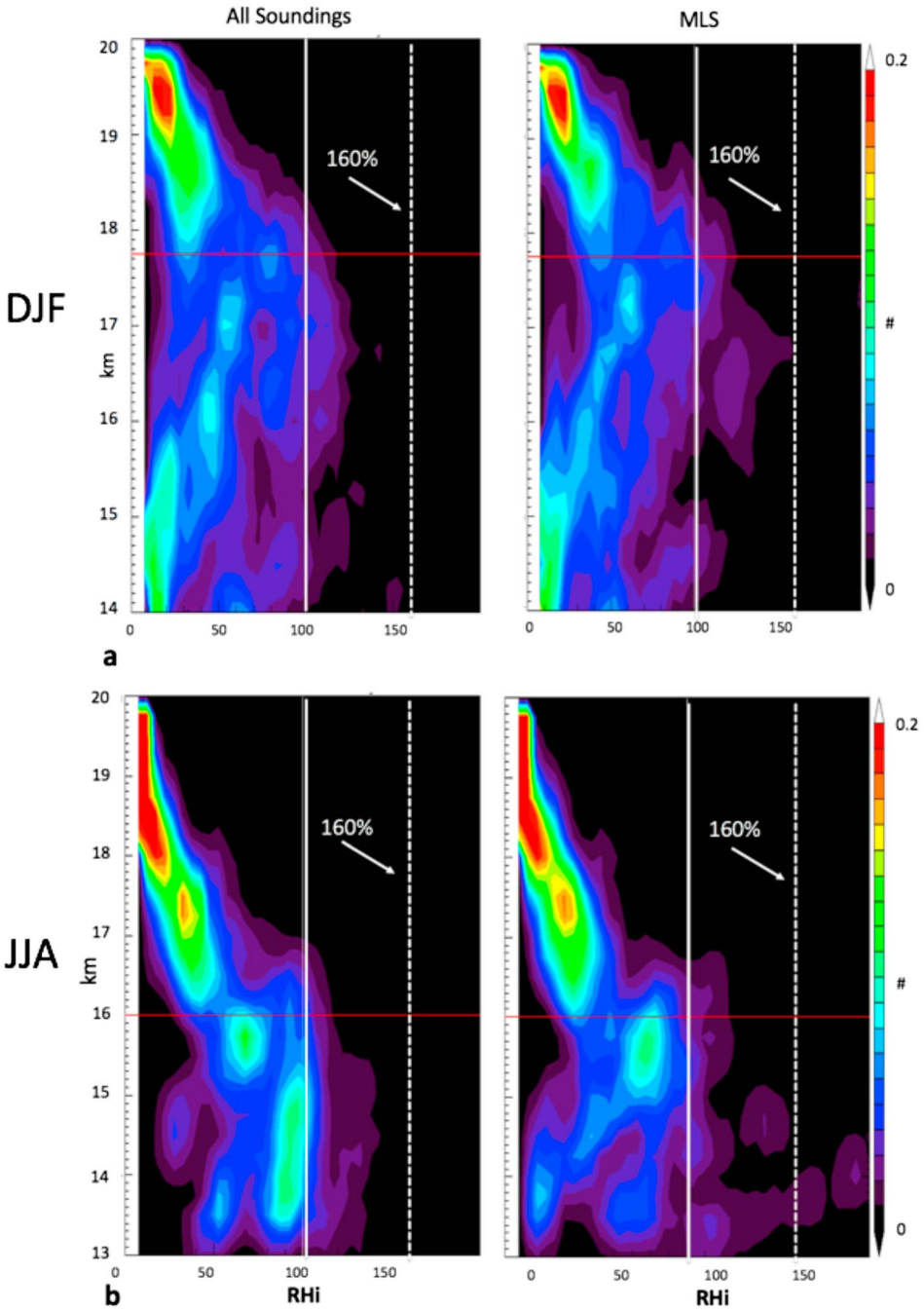

Figure 7. CFH balloon sonde RHi measurements from Costa Rica (left) and MLS (right) interpolated measurements at the same location. (a) The winter period; 20 sondes were composited. (b) The summer period; 24 sondes. Red line indicates the average position of the cold point tropopause. MLS = Microwave Limb Sounder; DJF = December–February; JJA = June–August; RHi = relative humidity with respect to ice.

to the convective heating (Kim et al., 2018). As mentioned above, the response forces Rossby and Kelvin waves that effectively extend the dynamical influence of convection to the east. The coldest region is located near 150°E bracketing the equator. Air is advected around the two high pressure systems and rides up the elevated isentropes into the cold region. This is the upward adiabatic transport. As air exits the cold region, it rides down the isentropes producing downward adiabatic transport seen over the Philippines and in the TEP. The downward adiabatic motion warms the air outside the cold region, lowering the RHi as seen in Figures 6a and 7a.

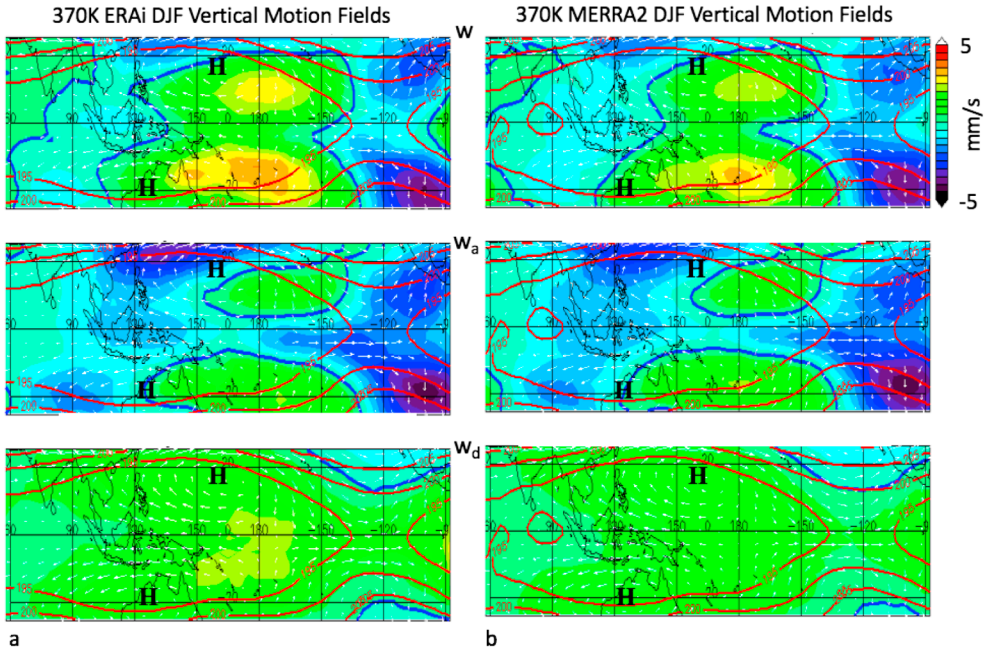

Figure 8. Five-year average of the 370 K (~107 hPa) DJF w fields in millimeters per second, (a) using ERA-Interim and (b) using MERRA2. Within each part, the top figure is the w field, the middle is w_a (adiabatic vertical motion), and the bottom is w_d (diabatic vertical motion); $w = w_a + w_d$. Red contours show the temperature (5-K intervals). The vectors show the monthly mean horizontal wind field at 370 K. The thick blue contour is $w = 0$. Longitude and latitude lines are indicated. The large H in each figure indicates the center of the high pressure system. ERAi = ERA-Interim; MERRA2 = Modern-Era Retrospective analysis for Research and Applications, Version 2; DJF = December–February.

The diabatic heating maximizes over the coldest region. The overall pattern for w is the same for both reanalyses, but the diabatic heating for ERAi is larger. Wright and Fueglistaler (2013) and Randel and Jensen (2013) compared the diabatic heating rates from a number of reanalyses models including MERRA and ERAi. They found that there is significant disagreement between models in the region below 100 hPa (~16 km). Our results at 370 K show relatively good agreement between the reanalysis fields although ERAi has slightly higher tropical tropospheric heating rates compared to MERRA2 above 200 hPa. These differences may be the result of difference in the treatment of clouds and water vapor in the radiative transfer models used in the reanalysis. Cloud heating is especially important (Corti et al., 2006; Yang et al., 2010), and a comparison made in Ueyama et al. (2015) shows that the heating rates calculated by Yang et al. (2010) using observed clouds are ~20% higher than MERRA heating rates in the winter TWP.

4.1. TTL Water Vapor Flux Constraints

In order to understand the basic water vapor/ice dynamics of the TTL, we derive some simple constraints in this section. These constraints set the basis for the simple models introduced in the next section. To begin, we assume for simplicity that all clouds in the TTL form as a result of in situ supersaturation and clouds are not associated with convection. A steady state model of the TTL would balance the upward flux of water vapor against the downward flux of ice by sedimentation. In other words, from continuity $\frac{\mathrm{d}}{\mathrm{dz}}\rho\mu w = \frac{\mathrm{d}}{\mathrm{dz}}\rho\mu_{\mathrm{i}}w_{\mathrm{s}}$ where μ is the water vapor mixing ratio, w_s is the Stokes sedimentation velocity, w is the upward velocity, μ_i is the mixing ratio of ice, and ρ is the air density. We can simply integrate the flux balance equation obtaining $\mu_i \sim \mu w/w_s$. Since w is usually much smaller than w_s, this equation produces the obvious result that only a small amount of falling ice is needed to balance the slower upward flux of water vapor. Now we can extend this equation further by assuming that the ice particles are approximately spheres, $\mu_i = Knr^3$ where r is the particle radius, n is the number density of particles, K is $4\eta\pi/3m$ where η is the atmospheric number density per mole and m is the molar mass of water vapor. The Stokes sedimentation velocity for spheres is given by $w_i = r^2\beta$ where $\beta = 2g(\rho_i - \rho)/(9\xi_a)$ where g is the gravitational acceleration, ρ_i is the density of ice, and ξ_a is viscosity of air. Substituting these terms, we obtain $n = w\mu/\beta Kr^5$. This equation states the obvious result that

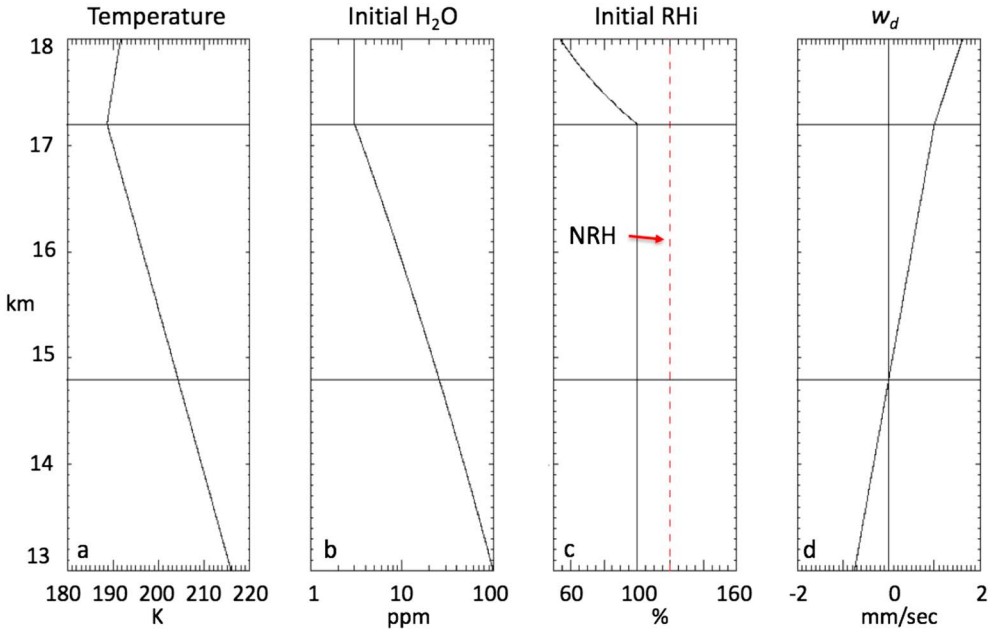

Figure 9. Initial profiles used in the bulk model. Left plot (a) shows the temperature profile—roughly a tropical standard atmosphere. Horizontal lines show the tropopause and base of the tropical tropopause layer. Plot (b) shows the initial water vapor mixing ratio. The water vapor mixing ratio is computed assuming that the profile has 100% RHi up to the tropopause. Above the tropopause, the water vapor is held fixed at tropopause value. Plot (c) shows the RHi. Plot (d) shows the diabatic vertical velocity used, which is 0 at the base of the tropical tropopause layer. The nucleation relative humidity is shown in plot c (red dashed line). RHi = relative humidity with respect to ice; NRH = nucleation RHi.

as the particle size increases, a smaller number of falling ice crystals is required to balance the upward water vapor flux. Observations indeed show very steep fall off in ice crystal number with respect to radius (Krämer et al., 2009, 2016; Lawson et al., 2008, 2010). Assuming that the functional form of the size distribution of ice crystals is determined by the nucleation and growth properties, not the vertical flux of water vapor (e.g., Heymsfield, 2007), we expect n itself to be proportional to the upward flux. In other words, n has to increase as the upward vapor flux increases in order keep the RHi from supersaturation. This connection is another way to look at the relationship between high CF, high RHi, and regions with high w—if the RHi in the TTL is held constant, increasing the upward flux of water will increase n, the CF.

4.2. A Time-Dependent 1-D Model of the TTL

The TTL can be further investigated using a one-dimensional "bulk" model that illustrates the competing processes of humidification, ice formation, and rehydration. For simplicity, we consider only the effects of the diabatic circulation at this point. Figure 9 shows the model set up. The temperature is the TWP average, and the w_d profile is the average diabatic vertical motion for the TWP region (±20° latitude and 130°–180° longitude) estimated from the heating rate, $w_d = \dot{\theta}\left(\frac{dz}{d\theta}\right)$ where θ is the potential temperature, $\dot{\theta}$ is the heating rate, and z is the log-pressure height as defined above. The vertical velocity is upward above about 14.8 km. In Figure 9c we show the initial RHi, which is set to 100% below the tropopause. From the RHi and temperature, we compute the water vapor concentration shown in Figure 9b. Above the tropopause (17.2 km) the water vapor concentration is held fixed at the tropopause value. The idea behind this assumption is that convection is supplying all the water vapor at the $w_d = 0$ level so the air is 100% saturated at the TTL base and below.

We compute the change in water vapor by integrating $\frac{\partial \mu}{\partial t} + w_d \frac{\partial \mu}{\partial z} = w_s \frac{\partial \mu_i}{\partial z} + S_i$ where S_i denotes the source or sink of water vapor due to the condensation and accumulation of ice or evaporation of existing ice. We first consider only the role of diabatic motion. For this model, we assume that the initial profile is at 100% RHi throughout the TTL. The nucleation RHi (NRH) threshold is set to 120% in this example to generate more frequent nucleation. When ice nucleates we assume that 2-μm-radius crystals form with sufficient

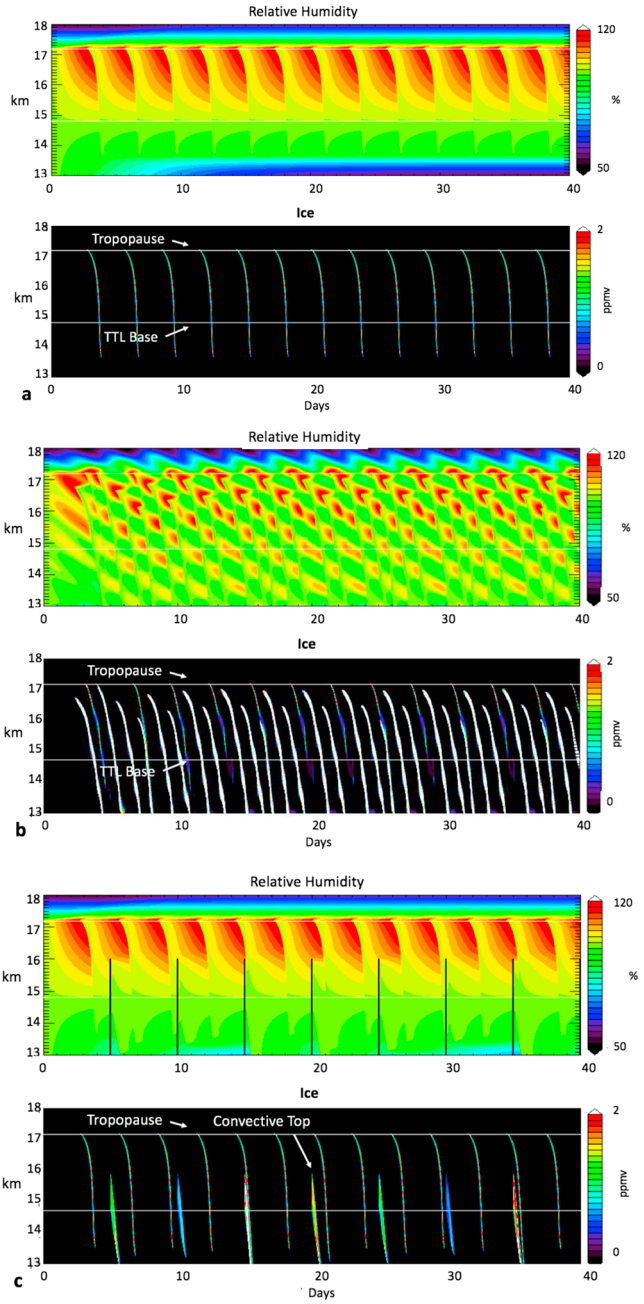

Figure 10. Time-dependent bulk model of the TTL. (a) No waves experiment. Upper figure shows the RHi; lower figure shows ice mixing ratio. The horizontal white horizontal lines define the upper and lower boundaries of the TTL. Once nucleated, ice particles fall through the TTL, decreasing RHi in the >100% RHi regions of the TTL and evaporating in the <100% RHi below the TTL. (b) A temperature oscillation is added simulating a gravity wave with an amplitude increasing with height. The temperature wave creates more nucleation events, and the ice mixing ratio is often above 2 ppmv producing white descending lines. (c) The impact of convection against the background of vertically advecting water. Convection is simulated by resetting the RHi to 100%. If the RHi is >100%, the excess water is converted to ice. Upper figure vertical black lines show the times convection is initiated. TTL = tropical tropopause layer.

number to bring the RHi down to100%. Ice falls at a speed of $w_s - w_d$ where w_s is the Stokes sedimentation velocity defined above. As the ice crystals grow or sublimate, the sedimentation speed is adjusted. As the ice falls, and if the local RHi is above 100%, the ice crystals will grow and deplete water vapor. If the local RHi is below 100%, ice will evaporate increasing the water vapor. The cloud physics modules used here are the same as those described in Schoeberl et al. (2014). The model has a 5-m vertical resolution and 50-s time step for numerical stability.

Figure 10a shows model results from a 40-day model integration with only the diabatic vertical velocity. Above the $w_d = 0$ level, water vapor is advected upward into colder layers and the RHi increases. Below the $w_d = 0$ level (the base of the TTL, 14.8 km here), downward advection of water vapor into warmer layers reduces the RHi. When the NRH limit is first exceeded near the tropopause, ice crystals form and begin to fall through the layers below. The ice crystals quickly grow to from 2 to >20 μm. The falling ice dehydrates the supersaturated layers in the TTL. Once the crystals fall below the TTL base, the ice begins to evaporate adding water to the lowest layers. The evaporation of ice extends the higher RHi region downward below the TTL base. With continued upward advection of water, the cycle begins again. In the TTL, periodic dehydration events occur about every 3 days. Note that falling ice increase the water vapor just below the TTL (not shown).

Gravity waves that occur in the TTL can also trigger nucleation events and such waves are included in models of the TTL (Jensen & Pfister, 2004; Schoeberl et al., 2016; Ueyama et al., 2015). Including gravity waves in the bulk model simulates the role of adiabatic motion. We introduce a temperature oscillation of the form $T' = T'_o e^{z/(2H)} \cos(2\pi(z/\lambda + t/\tau))$, where λ is the vertical wavelength (1 km) and τ is the period (3 days), $T'_o = 0.35$ K and z is defined above. This formula simulates the downward phase propagation and growth of gravity wave amplitude with altitude. The gravity wave is turned on over 3 days. Figure 10b shows the RHi and the increase in nucleation events that result from adding the gravity wave. The nucleation events occur at different altitudes with higher ice mixing ratio events occurring at lower altitudes where there is more water available to produce ice crystals.

A third simulation shown in Figure 10c shows the impact of convection. Convective events are initiated every 5 days periodically reaching from the base of the TTL to 16 km. Convection resets the RHi to 100%, and if RHi is >100%, the excess water is converted to ice. The convective ice crystals size is set to 10-μm radius. The number of crystals is determined by the available water exceeding 100% RHi. For this situation, convection is always dehydrating above the base of the TTL and hydrating below it through falling ice. The mixing ratio of convective ice falling through the TTL varies and is determined by the point in the periodic saturation cycle convection occurs.

Figure 11 summarizes the experiments. Figure 11a shows the average RHi, and Figure 11b shows the CF both averaged from day 15–40. Without waves, the average RHi in the TTL remains above 100% and the model predicts that the highest RHi will be close to the tropopause, decreasing rapidly above. The RHi below the TTL base is subsaturated due to diabatic descent. This relationship is also seen in the observations.

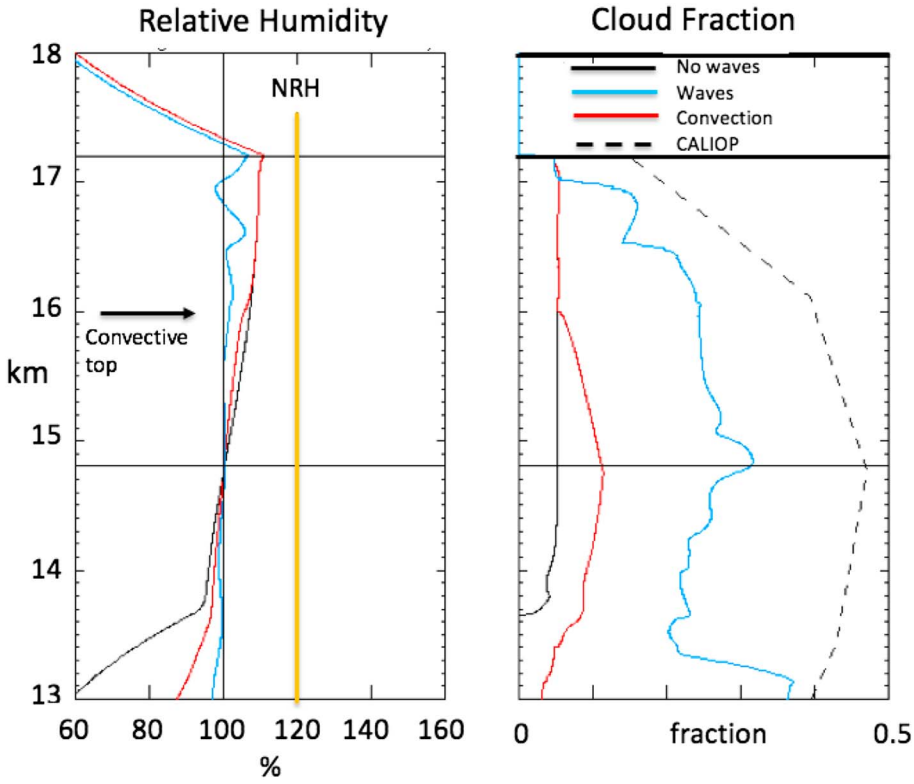

Figure 11. Averages of the tropical tropopause layer model shown in Figure 10 from days 15–40. Left figure shows the RHi. Solid black line is the average for the model where no convection is used, blue line is the wave case and the red line is the convection case, and the orange vertical line is the NRH. The right figure shows the cloud fraction. Horizontal black lines delineate the tropical tropopause layer region. The dashed line is the average cloud fraction from CALIOP within ±20° latitude of the equator. CALIOP = Cloud-Aerosol Lidar with Orthogonal Polarization; RHi = relative humidity with respect to ice; NRH = nucleation RHi.

The presence of waves significantly reduces the average RHi compared to the no-wave experiment as a result of the increase in dehydration events. More importantly, the increase in nucleation events significantly increases the CF, bringing it much closer to the CALIOP values and even simulating the functional dependence of the CALIOP CF with altitude. Finally, convection lowers the RHi below the convective top and increases RHi below the TTL base. Convection also produce an increase in the CF as expected.

Although the time dependent model is highly simplified, it provides important insights into the TTL hydrological cycle: (1) With the NRH threshold set above 100%, the TTL in our bulk model will be, on the average, supersaturated; (2) waves play an important role in amplifying the dehydration process and increasing CF; (3) convection dehydrates the region of supersaturation and increases clouds; and (4) short-term increases in RHi below the base of the TTL due to falling ice suggest that TTL may be an important source of water to the region below the TTL. We recognize that both adiabatic and diabatic motions in the TTL can locally be about twice as large as used in the bulk model (see Figure 8), which used a regional average. Increasing the vertical motion field will increase the frequency of nucleation events.

As is evident in Figures 4 and 5 a large portion of the TTL is subsaturated, so in this regard the bulk model only reproduces the supersaturated elements of the TTL. The TTL is not an isolated region and lateral transport of subsaturated air into the TTL or dehydration by convection will likely reduce the RHi. To address the more complicated situation, we use our FDF model to simulate the TTL and produce a more quantitative assessment of convective impact.

4.3. FDF Model Simulations

The FDF model is described in Schoeberl and Dessler (2011) and most recently in Schoeberl et al. (2016, 2018). Briefly, FDF is a Lagrangian domain filling model that includes convective saturation and a simple

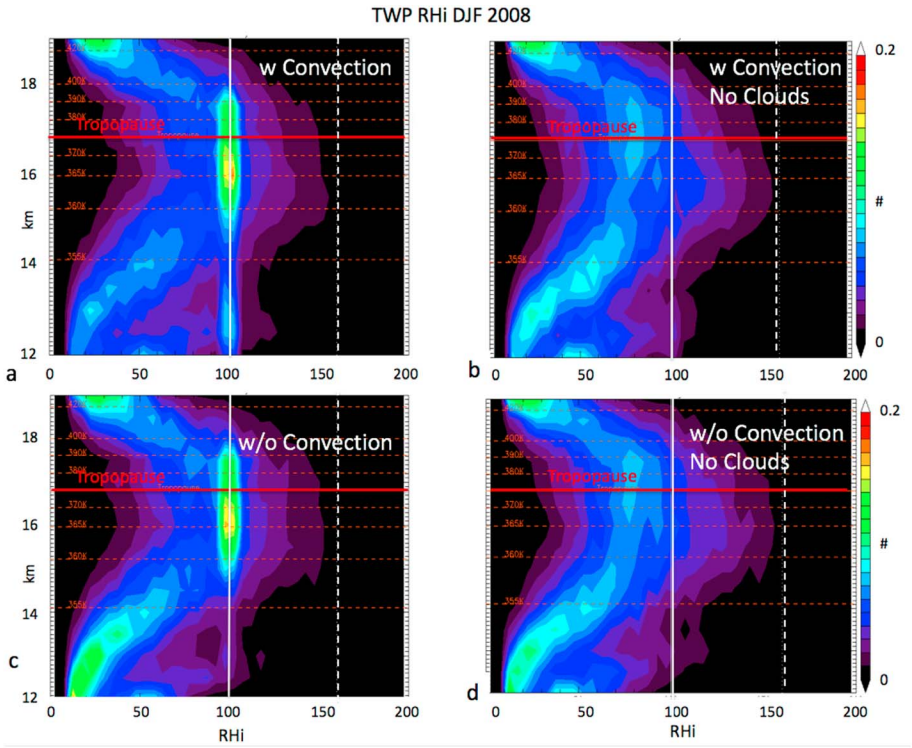

Figure 12. RHi probability density function from the forward domain-filling trajectory model simulation of the tropical tropopause layer for DJF 2008 over the TWP (110–160°E longitude, equatorward of 20°). Red line labeled "Tropopause" is the average tropopause height over the tropical region. Dashed lines are the average height of potential surfaces. The nucleation RHi is set to 160% for this simulation. (a, c) All trajectory points including cloudy ones. (b, d) Cloudy trajectories are removed. (a, b) For simulations that include convection. (c, d) Convection not included. Vertical white solid line is 100% RHi; the vertical white dashed line is 160% RHi. TWP = Tropical Western Pacific; RHi = relative humidity with respect to ice; DJF = December–February.

cloud physics scheme. The model uses hundreds of thousands of trajectory parcels to simulate upper tropospheric and stratospheric processes. The NRH is prescribed at 160% for the runs shown here to provide a case with high levels of supersaturation; FDF results for lower NRH values are described in Schoeberl et al. (2018, see Figure 3). Gravity waves are included in the simulation as also described in Schoeberl et al. (2016). Convection is included using the SC convective heights and measurements of convective ice number density and particle size from Frey et al. (2014). As shown in Schoeberl et al. (2018), the model results are in good agreement with both MLS and CALIOP observations of the TTL. Here we report two experiments to determine the impact of convection on the TTL saturation layer. In the two experiments, only the convection is

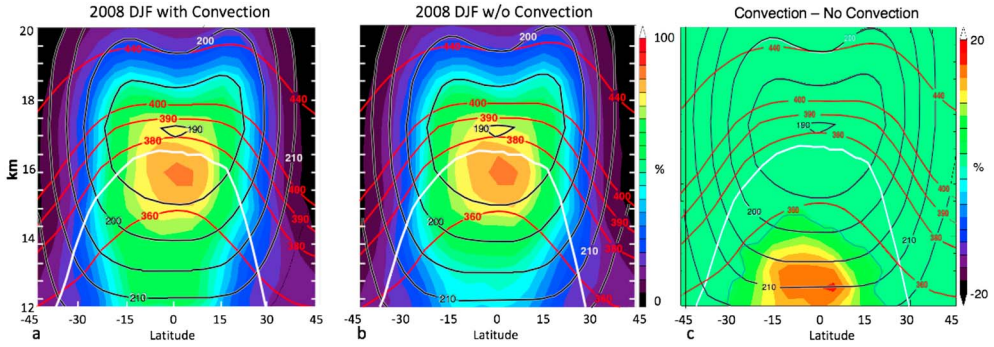

Figure 13. Forward domain-filling trajectory model zonal mean relative humidity with respect to ice. (a) Simulation with convection. (b) Simulation without convection. (c) The difference between a and b. The zonal average tropopause is thick white line. Temperatures are black lines, and the potential temperature are in red lines. The thin blue line in c indicates 0. DJF = December–February.

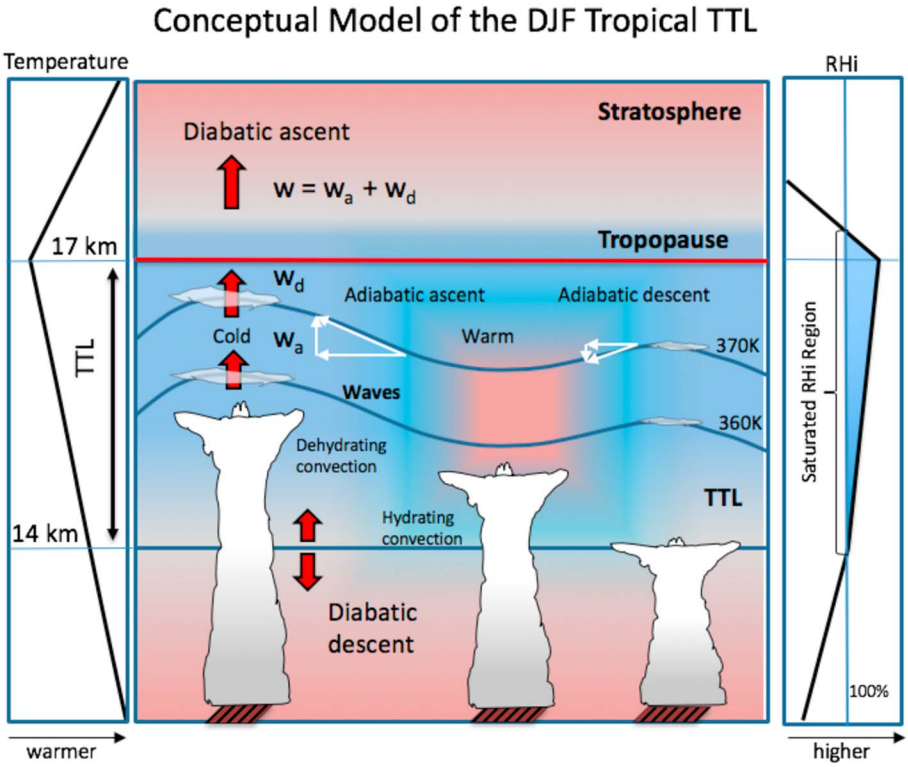

Figure 14. Conceptual model of the TTL Tropical Western Pacific dynamics. Convection provides moisture at the base of the TTL ($w_d = 0$). Convection penetrating above the base can dehydrate or hydrate depending on the local RHi. As air moves upward within the TTL as a result of diabatic heating (w_d), RHi increases. Adiabatic wave motions (w_a) can trigger local cloud formation, and falling ice also dehydrates the regions below the nucleation level. As air enters the stratosphere, warming temperatures reduces the RHi. DJF = December–February; TTL = tropical tropopause layer; RHi = relative humidity with respect to ice.

turned off and on; similar experiments were performed in Ueyama et al. (2015). The parcels are launched at 355 K with water vapor set to MLS zonal mean values.

Figure 12 shows the water vapor TWP PDF (with and without clouds) from the two simulations. The model agrees well with the aircraft observations shown in Figures 5a and 5b. High RHi points are seen above the tropopause as is observed, and the dry zone below about 14–15 km is also evident. The RHi increases slightly with altitude throughout the TTL as was seen in the bulk model. Comparing the convection and no-convection simulations shown in Figures 12a and 12c, we see an increase in 100% RHi values in the convective case below about 14 km (360 K). When clouds are not included in the PDF (Figures 12b and 12d), the impact of convection is even less apparent. This suggests that convection has little effect on the TWP TTL. To confirm this idea, Figure 13 shows the zonal mean RHi for the convection and no-convection simulations and their difference. The RHi plots are only different below ~14 km. Thus, in the FDF model, convection is supplying additional water vapor to the lower TTL, but convection is not playing much of a role in increasing the TTL RHi. There is also a very slight reduction in peak RHi for the convective case compared to the no convection case (note the location of the zero line in Figure 13c) suggesting that convection acts to reduce the RHi. These results are in line with the convective impact results reported by Schoeberl et al. (2018), Jensen, Thornberry, et al. (2017), and Ueyama et al. (2015).

5. Summary and Conclusions

High values of RHi appear to be a near permanent feature of the TTL in both summer and winter. This is evident in the MLS satellite data (Figures 2–4), aircraft measurements from the ATTREX, POSIDON (Figure 5; Jensen, Thornberry, et al., 2017), and other airborne missions (Krämer et al., 2009) as well as in

balloon data (Figure 7; see Selkirk et al., 2010). CALIOP observations shows the highest RHi tends to be colocated with clouds and loosely associated with convection (Figures 2 and 3).

The highest values of RHi are found in the winter TWP where diabatic heating is largest and temperatures are coldest. Regions of high RHi are also evident over South America and Africa as well as coincident with the Himalaya Monsoon during summer (Figure 3b). In these areas, the high humidity is more closely associated with convection. The TEP is less humid, and this likely results from adiabatic descent competing with the overall diabatic ascent (see 150°W, Figure 8, note the downward displacement of the potential temperature surfaces).

We hypothesize that the high values of TTL RHi are generated by diabatically rising air is advecting water upward into the colder upper troposphere (see Jensen, Thornberry, et al., 2017). Convection detraining between 14 and 15 km at the base of the TTL is the primary source of water for the TTL. Within the TTL upward advection leads to increasing RHi with altitude. When the local RHi value reaches cloud nucleation levels, ice crystals form, fall through the TTL, grow in saturated regions removing water vapor, and eventually sublimate below the TTL. Above the tropopause, RHi drops as stratospheric temperatures increase with altitude. Figure 14 summarizes this conceptual model.

To provide some quantification of the TWP TTL dehydration process, we introduce a bulk model of the TWP region using vertical velocities and temperatures from MERRA2 and a simplified ice model that includes ice nucleation, deposition, sublimation, and sedimentation. This model reproduces the many of the details of TWP observations described above. The TTL's lower boundary is the $w_d \sim 0$ surface, which is set to 100% RHi. Air moving downward below that boundary will warm, and the RHi will decrease; air above the TTL base moves upward and RHi increases. Once the RHi reaches the nucleation limit, ice forms and falls through the layer, dehydrating the layers RHi as vapor condenses on the falling ice crystals. As ice falls below the base of the TTL, it evaporates in the drier layers. Continued upward advection of water vapor within the TTL starts the process all over again. This periodic formation of ice is controlled by the NRH. When temperature waves are added to the model to simulate adiabatic motion, more frequent nucleation events occur, which decreases the average RHi and significantly increases CF.

Both adiabatic and diabatic motions contribute to the dynamics of the cloud formation processes within the TTL (Figure 8). At the edges of the TWP TTL cold region, air is advected horizontally, rises adiabatically, and cools and the RHi increases to saturation levels. Over the TWP cold region (where the potential temperature surfaces are relatively flat), diabatic vertical velocity is highest and air is carried upward into a colder environment across the isentropes toward the tropopause. The adiabatic and diabatic motion fields are comparable, although the adiabatic motions are stronger at the edge of the cold region. Note that we find some disagreement between the diabatic heating rates between MERRA2 and ERAi; ERAi diabatic motion being slightly stronger. This disagreement was also noted by Wright and Fueglistaler (2013). On the winter TEP side, air moves along the isentropes downward, overwhelming the upward diabatic motion; the air warms and the RHi falls below 100% on the average (see Figures 8, 6b, and 7b).

In the bulk model, convection that penetrates to the mid-TTL does not affect the cycle of nucleation and rehydration above the convective top. Below the convective top, convection dehydrates the TTL—saturation levels are reduced to 100%. To more precisely investigate the role of convection, we use the FDF trajectory model that includes satellite based convective. Consistent with our simple model, the FDF model results show that convective hydration/dehydration is only important in the region where convection is frequent —below ~14 km. Our results are contingent on the altitude distribution of SC convection, which has not been extensively validated. As a final caveat, we have focused mostly on the winter TWP during normal conditions. Our conclusions about the role of convection mostly describe that region and are not likely to apply to anomalous situations such as El Niño (Avery et al., 2017; Ye et al., 2018), to the summer TTL nor to saturated regions observed near the Asian monsoon. Indeed, Figure 3b suggests that in the summer months, convection in the Asian monsoon region is more closely tied to the highest RHi region consistent with the findings of Ueyama et al. (2018).

Because the tropical upper troposphere is an important component of the Earth's climate system, accurate simulations of climate feedbacks tied to this region are critical. Climate model scenarios where the

convective heights or convective frequency increase as a result of surface warming could alter the RHi in the TTL and the concomitant CF and could ultimately drive a stratospheric water vapor feedback (Dessler et al., 2013). Likewise, widening of the tropical region (e.g., Seidel & Randel, 2007) may also increase the tropical cirrus shield and alter the radiation balance.

Acknowledgments
CALIOP, MLS, and MERRA2 data used in this study are publicly available from NASA. Satellite convection data sets are available through L. Pfister (leonhard.pfister@nasa.gov). Aircraft data are available from the NASA Earth Science Project Office (https://espo.nasa.gov/). Ticosonde water vapor soundings are archived with the Network for Detection of Atmospheric Composition Change (NDACC) at https://www.ndsc.ncep.noaa.gov/data/. The authors would like to thank J. Kummer and the reviewers for helpful comments on this paper and suggested changes. We would also like to thank B. Schoeberl for improving the figures. This work was supported under NASA grant 80NSSC18K0134. Ticosonde water vapor observations in Costa Rica are supported by the NASA Radiation Sciences and Upper Atmosphere Research Program.

References

Avery, M. A., Davis, S., Rosenlof, K., Ye, H., & Dessler, A. E. (2017). Large anomalies in lower stratospheric water vapour and ice during the 2015-2016 El Niño. *Nature Geoscience*, *10*(6), 405–409. https://doi.org/10.1038/NGEO2961

Boucher, O., Randall, D., Artaxo, P., Bretherton, C., Feingold, G., Forster, P., et al. (2013). Clouds and aerosols. In T. F. Stocker et al. (Eds.), *Climate change 2013: The physical science basis. Contribution of Working Group I to the Fifth Assessment Report of the Intergovernmental Panel on Climate Change* (pp. 571–657). Cambridge, UK: Cambridge University Press. https://doi.org/10.1017/CBO9781107415324.016

Carminati, F., Ricaud, P., Pommereau, J.-P., Rivière, E., Khaykin, S., Attié, J.-L., & Warner, J. (2014). Impact of tropical land convection on the water vapour budget in the tropical tropopause layer. *Atmospheric Chemistry and Physics*, *14*(12), 6195–6211. https://doi.org/10.5194/acp-14-6195-2014

Cooney, J. W., Bowman, K. P., Homeyer, C. R., & Fenske, T. M. (2018). Ten year analysis of tropopause-overshooting convection using GridRad data. *Journal of Geophysical Research: Atmospheres*, *123*, 329–343. https://doi.org/10.1002/2017JD027718

Corti, T., Luo, B. P., de Reus, M., Brunner, D., Cairo, F., Mahoney, M. J., et al. (2008). Unprecedented evidence for deep convection hydrating the tropical stratosphere. *Geophysical Research Letters*, *35*, L10810. https://doi.org/10.1029/2008GL033641

Corti, T., Luo, B. P., Fu, Q., Vömel, H., & Peter, T. (2006). The impact of cirrus clouds on tropical troposphere-to-stratosphere transport. *Atmospheric Chemistry and Physics*, *6*, 2539–2547.

Dee, D. P., Uppala, S. M., Simmons, A. J., Berrisford, P., Poli, P., Kobayashi, S., et al. (2011). The ERA-Interim reanalysis: Configuration and performance of data assimilation system. *Quarterly Journal of the Royal Meteorological Society*, *137*(656), 553–597. https://doi.org/10.1002/qj.828

Dessler, A. E., Hanisco, T. F., & Fueglistaler, S. (2007). Effects of convective ice lofting on H2O and HDO in the tropical tropopause layer. *Journal of Geophysical Research*, *112*, D18309. https://doi.org/10.1029/2007JD008609

Dessler, A. E., Schoeberl, M. R., Wang, T., Davis, S. M., & Rosenlof, K. H. (2013). Stratospheric water vapor feedback. *Proceedings of the National Academy of Sciences of the United States of America*, *110*, 18,087–18,091. https://doi.org/10.1073/pnas.1310344110

Dessler, A. E., Ye, H., Wang, T., Schoeberl, M. R., Oman, L. D., Douglass, A. R., et al. (2016). Transport of ice into the stratosphere and the humidification of the stratosphere over the 21st century. *Geophysical Research Letters*, *43*, 2323–2329. https://doi.org/10.1002/2016GL067991

Folkins, I., Kelly, K., & Weinstock, E. (2002). A simple explanation for the increase in relative humidity between 11 and 14 km in the tropics. *Journal of Geophysical Research*, *107*(D23), 4736. https://doi.org/10.1029/2002JD002185

Frey, W., Borrmann, S., Fierli, F., Weigel, R., Mitev, V., Matthey, R., et al. (2014). Tropical deep convective life cycle: Cb-anvil cloud microphysics from high-altitude aircraft observations. *Atmospheric Chemistry and Physics*, *14*(23), 13,223–13,240. https://doi.org/10.5194/acp-14-13223-2014

Fueglistaler, S., Dessler, A. E., Dunkerton, T. J., Folkins, I., Fu, Q., & Mote, P. W. (2009). The tropical tropopause layer. *Reviews of Geophysics*, *47*, RG1004. https://doi.org/10.1029/2008RG000267

Gelaro, R., McCarty, W., Suárez, M. J., Todling, R., Molod, A., Takacs, L., et al. (2017). The Modern-Era Retrospective Analysis for Research and Applications, Version 2 (MERRA-2). *Journal of Climate*, *30*(14), 5419–5454. https://doi.org/10.1175/jcli-d-16-0758.1

Gettelman, A., Randel, W. J., Wu, F., & Massie, S. T. (2002). Transport of water vapor in the tropical tropopause layer. *Geophysical Research Letters*, *29*(1), 1009. https://doi.org/10.1029/2001GL013818

Gill, A. E. (1980). Some simple solutions for heat-induced tropical circulations. *Quarterly Journal of the Royal Meteorological Society*, *106*(449), 447–462. https://doi.org/10.1002/qj.49710644905

Haladay, T., & Stephens, G. (2009). Characteristics of tropical thin cirrus clouds deduced from joint CloudSat and CALIPSO observations. *Journal of Geophysical Research*, *114*, D00A25. https://doi.org/10.1029/2008JD010675

Heymsfield, A. J. (2007). On measurements of small ice particles in clouds. *Geophysical Research Letters*, *34*, L23812. https://doi.org/10.1029/2007GL030951

Holton, J. R., & Gettelman, A. (2001). Horizontal transport and dehydration in the stratosphere. *Geophysical Research Letters*, *28*, 2799–2802. https://doi.org/10.1029/2001GL013148

Huffman, G. J., Adler, R. F., Bolvin, D. T., & Nelkin, E. J. (2010). The TRMM Multi-satellite Precipitation Analysis (TMPA). In F. Hossain & M. Gebremichael (Eds.), chap. 1*Satellite Applications for Surface Hydrology* (pp. 3–22). New York: Springer. https://doi.org/10.1007/978-90-481-2915-7_1

Intergovernmental Panel on Climate Change (IPCC) (2013). Climate Change 2013: The Physical Science Basis. In T. F. Stocker et al. (Eds.), Contribution of Working Group I to the Fifth Assessment Report of the Intergovernmental Panel on Climate Change (1535 pp.). Cambridge, UK, and New York. Cambridge University Press.

Jensen, E. J., Ackerman, A. S., & Smith, J. A. (2007). Can overshooting convection dehydrate the tropical tropopause layer? *Journal of Geophysical Research*, *112*, D11209. https://doi.org/10.1029/2006JD007943

Jensen, E. J., & Pfister, L. (2004). Transport and freeze-drying in the tropical tropopause layer. *Journal of Geophysical Research*, *109*, D02207. https://doi.org/10.1029/2003JD004022

Jensen, E. J., Pfister, L., Ackerman, A. S., Tabazadeh, A., & Toon, O. B. (2001). A conceptual model of the dehydration of air due to freeze-drying by optically thin, laminar cirrus rising slowly across the tropical tropopause. *Journal of Geophysical Research*, *106*(D15), 17,237–17,252. https://doi.org/10.1029/2000JD900649

Jensen, E. J., Pfister, L., Jordan, D. E., Bui, T. V., Ueyama, R., Singh, H. B., et al. (2017). The NASA Airborne Tropical TRopopause EXperiment (ATTREX): High-altitude aircraft measurements in the tropical western Pacific. *Bulletin of the American Meteorological Society*, *98*(1), 129–143. https://doi.org/10.1175/BAMS-D-14-00263.1

Jensen, E. J., Read, W. G., Mergenthaler, J., Sandor, B. J., Pfister, L., & Tabazadeh, A. (1999). High humidities and subvisible cirrus near the tropical tropopause. *Geophysical Research Letters*, *26*(15), 2347–2350. https://doi.org/10.1029/1999GL900266

Jensen, E. J., Thornberry, T. D., Rollins, A. W., Ueyama, R., Pfister, L., Bui, T., et al. (2017). Physical processes controlling the spatial distributions of relative humidity in the tropical tropopause layer over the Pacific. *Journal of Geophysical Research: Atmospheres*, *122*, 6094–6107. https://doi.org/10.1002/2017JD026632

Johnston, B. R., Xie, F., & Liu, C. (2018). The effects of deep convection on regional temperature structure in the tropical upper troposphere and lower stratosphere. *Journal of Geophysical Research: Atmospheres*, *123*, 1585–1603. https://doi.org/10.1002/2017JD027120

Kelly, K. K., Profitt, M. H., Chan, K. R., Loewenstein, M., Podolske, J. R., Strahan, S. E., et al. (1993). Water vapor and cloud water measurements over Darwin during STEP 1987 tropical mission. *Journal of Geophysical Research*, *98*(D5), 8713–8723. https://doi.org/10.1029/92JD02526

Khaykin, S., Pommereau, J.-P., Korshunov, L., Yushkov, V., Nielsen, J., Larsen, N., et al. (2009). Hydration of the lower stratosphere by ice crystal geysers over land convective systems. *Atmospheric Chemistry and Physics*, *9*(6), 2275–2287. https://doi.org/10.5194/acp-9-2275-2009

Khaykin, S. M., Pommereau, J.-P., & Hauchecorne, A. (2013). Impact of land convection on temperature diurnal variation in the tropical lower stratosphere inferred from COSMIC GPS radio occultations. *Atmospheric Chemistry and Physics*, *13*, 6391–6402. https://doi.org/10.5194/acp13-6391-2013

Kim, J., Randel, W. J., & Birner, T. (2018). Convectively driven tropopause-level cooling and its influences on stratospheric moisture. *Journal of Geophysical Research: Atmospheres*, *123*, 590–606. https://doi.org/10.1002/2017JD027080

Krämer, M., Rolf, C., Luebke, A., Afchine, A., Spelten, N., Costa, A., et al. (2016). A microphysics guide to cirrus clouds—Part 1: Cirrus types. *Atmospheric Chemistry and Physics*, *16*, 3463–3483.

Krämer, M., Schiller, C., Afchine, A., Bauer, R., Gensch, I., Mangold, A., et al. (2009). Ice supersaturations and cirrus cloud crystal numbers. *Atmospheric Chemistry and Physics*, *9*, 3505–3522. https://doi.org/10.5194/acp-9-3505-2009

Lawson, R. P., Jensen, E., Mitchell, D. L., Baker, B., Mo, Q., & Pilson, B. (2010). Microphysical and radiative properties of tropical clouds investigated in TC4 and NAMMA. *Journal of Geophysical Research*, *115*, D00J08. https://doi.org/10.1029/2009JD013017

Lawson, R. P., Pilson, B., Baker, B., Mo, Q., Jensen, E., Pfister, L., & Bui, P. (2008). Aircraft measurements of microphysical properties of subvisible cirrus in the tropical tropopause layer. *Atmospheric Chemistry and Physics*, *8*, 1609–1620. https://doi.org/10.5194/acp-8-1609-2008

Liu, C., & Zipser, E. J. (2005). Global distribution of convection penetrating the tropical tropopause. *Journal of Geophysical Research*, *110*, D23104. https://doi.org/10.1029/2005JD006063

Livesey, N., W. G. Read, P.A. Wagner, L. Froidevaux, A. Lambert, G. L. Manney, et al. (2017). Aura Microwave Limb Sounder (MLS) version 4.2x level 2 data quality and description document, JPL D-33509 Rev. C.

Minschwaner, K., & Dessler, A. E. (2004). Water vapor feedback in the tropical upper troposphere: Model results and observations. *Journal of Climate*, *17*, 1272–1282. https://doi.org/10.1175/1520-0442(2004)017,1272:WVFITT.2.0.CO;2

Molod, A., Takacs, L., Suarez, M., & Bacmeister, J. (2015). Development of the GEOS-5 atmospheric general circulation model: Evolution from MERRA to MERRA-2. *Geoscientific Model Development*, *85*(5), 1339–1356. https://doi.org/10.5194/gmd-8-1339-2015

Moyer, E., Irion, F., Yung, Y., & Gunson, M. (1996). ATMOS stratospheric deuterated water and implications for troposphere-stratosphere transport. *Geophysical Research Letters*, *23*(17), 2385–2388. https://doi.org/10.1029/96GL01489

Murphy, D. M., & Koop, T. (2005). Review of the vapor pressures of ice and supercooled water for atmospheric applications. *Quarterly Journal of the Royal Meteorological Society*, *131*, 1539–1565.

Newell, R. E., Zhu, Y., Browell, E. V., Ismail, S., Read, W. G., Waters, J. W., et al. (1996). Upper tropospheric water vapor and cirrus: Comparison of DC-8 observations, preliminary UARS microwave limb sounder measurements and meteorological analyses. *Journal of Geophysical Research*, *101*, 1931–1941.

Pfister, L., Selkirk, H. B., Jensen, E. J., Schoeberl, M. R., Toon, O. B., Browell, E. V., et al. (2001). Aircraft observations of thin cirrus clouds near the tropical tropopause. *Journal of Geophysical Research*, *106*(D9), 9765–9786. https://doi.org/10.1029/2000JD900648

Randel, W., & Jensen, E. (2013). Physical processes in the tropical tropopause layer and their roles in a changing climate. *Nature Geoscience*, *6*(3), 169–176. https://doi.org/10.1038/NGEO1733

Randel, W. J., Wu, F., & Rios, W. R. (2003). Thermal variability of the tropical tropopause region derived from GPS/MET observations. *Journal of Geophysical Research*, *108*(D11), 4024. https://doi.org/10.1029/2002JD002595

Rollins, A. W., Thornberry, T. D., Gao, R. S., Woods, S., Lawson, R. P., Bui, T. P., et al. (2016). Observational constraints on the efficiency of dehydration mechanisms in the tropical tropopause layer. *Geophysical Research Letters*, *43*, 2912–2918. https://doi.org/10.1002/2016GL067972

Romps, D. M. (2014). An analytical model for the tropical relative humidity. *Journal of Climate*, *27*. https://doi.org/10.1175/JCLI-D-14-00255.1

Russell, J. M. III, Gordley, L. L., Park, J., Drayson, R., Hesketh, W. D., Cicerone, R. J., et al. (1993). The Halogen Occultation Experiment (HALOE). *Journal of Geophysical Research*, *98*(D6), 10,777–10,797. https://doi.org/10.1029/93JD00799

Sassen, K., Wang, Z., & Liu, D. (2009). Cirrus clouds and deep convection in the tropics: Insights from CALIPSO and CloudSat. *Journal of Geophysical Research*, *114*, D00H06. https://doi.org/10.1029/2009JD011916

Schoeberl, M., Dessler, A., Ye, H., Wang, T., Avery, M., & Jensen, E. J. (2016). The impact of gravity waves and cloud nucleation threshold on stratospheric water and tropical tropospheric cloud fraction. *Earth and Space Science*, *3*, 295–305. https://doi.org/10.1002/2016EA000180

Schoeberl, M. R., & Dessler, A. E. (2011). Dehydration of the stratosphere. *Atmospheric Chemistry and Physics*, *11*, 8433–8446. https://doi.org/10.5194/ASC-11-8433-2011

Schoeberl, M. R., Dessler, A. E., Wang, T., Avery, M. A., & Jensen, E. J. (2014). Cloud formation, convection, and stratospheric dehydration. *Earth and Space Science*, *1*, 1–17. https://doi.org/10.1002/2014EA000014

Schoeberl, M. R., Jensen, E. J., Pfister, L., Ueyama, R., Avery, M., & Dessler, A. E. (2018). Convective hydration of the upper troposphere and lower stratosphere. *Journal of Geophysical Research: Atmospheres*, *123*, 4583–4593. https://doi.org/10.1029/2018JD028286

Schoeberl, M. R., Jensen, E. J., & Woods, S. (2015). Gravity waves amplify upper tropospheric dehydration by clouds. *Earth and Space Science*, *2*, 485–500. https://doi.org/10.1002/2015EA000127

Schoeberl, M. R., & Newman, P. A. (1995). A multiple-level trajectory analysis of vortex filaments. *Journal of Geophysical Research*, *100*, 25,801–25,815. https://doi.org/10.1029/95JD02414

Seidel, D. J., & Randel, W. J. (2007). Recent widening of the tropical belt: Evidence from tropopause observations. *Journal of Geophysical Research*, *112*, D20113. https://doi.org/10.1029/2007JD008861

Seidel, D. J., Ross, R. J., Angell, J. K., & Reid, G. C. (2001). Climatological characteristics of the tropical tropopause as revealed by radiosondes. *Journal of Geophysical Research*, *106*(D8), 7857–7878. https://doi.org/10.1029/2000JD900837

Selkirk, H. B., Vömel, H., Valverde Canossa, J. M., Pfister, L., Diaz, J. A., Fernández, W., et al. (2010). Detailed structure of the tropical upper troposphere and lower stratosphere as revealed by balloon sonde observations of water vapor, ozone, temperature, and winds during the NASA TCSP and TC4 campaigns. *Journal of Geophysical Research*, *115*, D00J19. https://doi.org/10.1029/2009JD013209

Sherwood, S. C., Chae, J.-H., Minnis, P., & McGill, M. (2004). Underestimation of deep convective cloud tops by thermal imagery. *Geophysical Research Letters*, *31*, L11102. https://doi.org/10.1029/2004GL019699

Thornberry, T. D., Rollins, A. W., Gao, R. S., Watts, L. A., Ciciora, S. J., McLaughlin, R. J., & Fahey, D. W. (2015). A two-channel, tunable diode laser-based hygrometer for measurement of water vapor and cirrus cloud ice water content in the upper troposphere and lower stratosphere. *Atmospheric Measurement Techniques*, *8*, 211–244.

Ueyama, R., Jensen, E. J., & Pfister, L. (2018). Convective influence on the humidity and clouds in the tropical tropopause layer during boreal summer. *Journal of Geophysical Research: Atmospheres*, *123*, 7576–7593. https://doi.org/10.1029/2018JD028674

Ueyama, R., Jensen, E. J., Pfister, L., & Kim, J.-E. (2015). Dynamical, convective, and microphysical control on wintertime distributions of water vapor and clouds in the tropical tropopause layer. *Journal of Geophysical Research: Atmospheres*, *120*, 10,483–10,500. https://doi.org/10.1002/2015JD023318

Vömel, H., David, D. E., & Smith, K. (2007). Accuracy of tropospheric and stratospheric water vapor measurements by the cryogenic frost point hygrometer: Instrumental details and observations. *Journal of Geophysical Research*, *112*, D08305. https://doi.org/10.1029/2006JD007224

Vömel, H., Oltmans, S. J., Johnson, B. J., Hasebe, F., Shiotani, M., Fujiwara, M., et al. (2002). Balloon-borne observations of water vapor and ozone in the tropical upper troposphere and lower stratosphere. *Journal of Geophysical Research*, *107*(8), 4210. https://doi.org/10.1029/2001JD000707

Wang, T., & Dessler, A. E. (2012). Analysis of cirrus in the tropical tropopause layer from CALIPSO and MLS data: A water perspective. *Journal of Geophysical Research*, *117*, D04211. https://doi.org/10.1029/2011JD016442

Woods, S., Lawson, R. P., Jensen, E., Bui, T. P., Thornberry, T., Rollins, A., et al. (2018). Microphysical properties of tropical tropopause layer cirrus. *Journal of Geophysical Research: Atmospheres*, *123*, 6053–6069. https://doi.org/10.1029/2017JD028068

Wright, J. S., & Fueglistaler, S. (2013). Large differences in reanalyses of diabatic heating in the tropical upper troposphere and lower stratosphere. *Atmospheric Chemistry and Physics*, *13*, 9565–9576. https://doi.org/10.5194/acp-13-9565-2013

Yang, Q., Fu, Q., & Hu, Y. (2010). Radiative impacts of clouds in the tropical tropopause layer. *Journal of Geophysical Research*, *15*, D00H12. https://doi.org/10.1029/2009JD012393

Ye, H., Dessler, A. E., & Yu, W. (2018). Effects of convective ice evaporation on interannual variability of tropical tropopause layer water vapor. *Atmospheric Chemistry and Physics*, *18*, 4425–4437. https://doi.org/10.5194/acp-18-4425-2018

Zahn, A., Christner, E., van Velthoven, P. F. J., Rauthe-Schöch, A., & Brenninkmeijer, C. A. M. (2014). Processes controlling water vapor in the upper troposphere/lowermost stratosphere: An analysis of 8 years of monthly measurements by the IAGOS-CARIBIC observatory. *Journal of Geophysical Research: Atmospheres*, *119*, 11,505–11,525. https://doi.org/10.1002/2014JD021687

Zhou, C., Dessler, A. E., Zelinka, M. D., Yang, P., & Wang, T. (2014). Cirrus feedback on interannual climate fluctuations. *Geophysical Research Letters*, *41*, 9166–9173. https://doi.org/10.1002/2014GL062095